Vortex-dynamical implications of nonmonotonic viscous dissipation of off-center droplet bouncing (F)

(iD) Chengming He (何成明), (iD) Xi Xia (夏溪) and (iD) Peng Zhang (张鹏)

COLLECTIONS

(F) This paper was selected as Featured

View Online   Export Citation   CrossMark

ARTICLES YOU MAY BE INTERESTED IN

Non-monotonic viscous dissipation of bouncing droplets undergoing off-center collision
Physics of Fluids **31**, 052004 (2019); https://doi.org/10.1063/1.5088544

Direct numerical simulation of multiscale flow physics of binary droplet collision
Physics of Fluids **32**, 062103 (2020); https://doi.org/10.1063/5.0006695

Coalescence dynamics of a droplet on a sessile droplet
Physics of Fluids **32**, 012104 (2020); https://doi.org/10.1063/1.5129901

AIP Publishing

Vortex-dynamical implications of nonmonotonic viscous dissipation of off-center droplet bouncing Ⓕ

View Online   Export Citation   CrossMark

Chengming He (何成明), 🆔 Xi Xia (夏溪), 🆔 and Peng Zhang (张鹏)[a] 🆔

AFFILIATIONS

Department of Mechanical Engineering, The Hong Kong Polytechnic University, Hung Hom, Kowloon 999077, Hong Kong

[a] Author to whom correspondence should be addressed: pengzhang.zhang@polyu.edu.hk

ABSTRACT

In this paper, vortex-dynamical perspectives were adopted to interpret the recently reported observation that the total viscous dissipation of off-center droplet bouncing varies nonmonotonically with the impact parameter [C. He, X. Xia, and P. Zhang, "Non-monotonic viscous dissipation of bouncing droplets undergoing off-center collision," Phys. Fluids **31**, 052004 (2019)]. The particular interest of this study is on analyzing the velocity and vorticity vector fields and their correlations, such as helicity and enstrophy. The helicity analysis identifies a strong interaction between the "ring-shaped" vortices and the "line-shaped" shear layers in the non-axisymmetric droplet internal flow. A general relation between the total enstrophy and the total viscous dissipation rate for an unsteady free-surface flow was theoretically derived and numerically verified. It shows that the equality between the total enstrophy and the total viscous dissipation rate holds for a single-phase flow confined by stationary boundaries but is not satisfied for a gas–liquid two-phase flow due to the interfacial movement. Both the total enstrophy and a defined "half-domain" helicity show the nonmonotonic variation with the impact parameter, implying their interrelation with the nonmonotonic viscous dissipation.

Published under license by AIP Publishing. https://doi.org/10.1063/5.0003057

I. INTRODUCTION

Collision of two liquid droplets in a gaseous environment occurs frequently in many natural and industrial processes involving dispersed gas–liquid two-phase flows. A large number of experimental studies on the droplet collision have been reported in the literature[1–11] and summarized in a few excellent reviews.[12–14] The majority of the previous studies[4,5,9–11] were focused on identifying and interpreting various outcomes of droplet collision, such as coalescence, bouncing, separation, and shattering.[15,16]

Extensive studies have been done to investigate the influence of a few controlling parameters on the collision outcomes. The widely adopted parameters are the collision Weber number, We, which measures the relative importance of the droplet inertia compared to the surface tension; the droplet Ohnesorge number, Oh, which measures the relative importance of the liquid viscous stress compared to the capillary pressure;[10,11,17,18] and the size ratio, Δ, for the influence of size disparity.[3,8,19–23] The collision outcomes can also be

significantly affected by the gas environment as such increasing the gas pressure promotes droplet bouncing and decreasing the gas pressure promotes droplet coalescence.[4,5] A practically significant implication of the gas pressure effect is that colliding fuel droplets tend to bounce off under high pressure in real combustion chambers, and it has been verified both experimentally and numerically.[24–26]

In addition to the above list of controlling parameters, the impact parameter, B, which measures the deviation of the trajectory of droplets ($B \leq 1$) from that of the head-on collision ($B = 0$), has been taken into account since the very beginning of the drop collision study,[1,2] manifested by the well-known collision nomogram in the $We - B$ parameter space and its many variants. Although it has been fully recognized that the impact parameter has a significant influence on the collision outcomes, its role is insufficiently and often intuitively understood, for example, through the effective collision Weber number, $We_{\text{eff}} = We(1 - B^2)$, because it produces the correct limiting cases for head-on collision ($B = 0$) and grazing collision ($B = 1$).

In the authors' recent computational study[27] about the off-center collision of two liquid droplets of equal size, the total viscous dissipation (TVD for short hereinafter) during droplet bouncing does not linearly depend on We_{eff}. Instead, a nonmonotonic TVD with varying B was discovered and verified. Specifically, a prolonged entanglement time and an enhanced internal-flow-induced viscous dissipation were found for bouncing droplets at intermediate B, compared with those at smaller or larger B. This was understood as the competition between the viscous dissipation rates (VDR for short hereinafter) induced by normal strains and shear strains. Fixing We while increasing B from 0 to 1, the VDR in the droplet interior being away from the interaction region decreases because of the reduced droplet deformation (mainly due to the decreased We_{eff}), whereas the VDR in the vicinity of the droplet interaction region increases, owing to the enhanced droplet shear flow. The competition between these two parts of VDR accounts for the enhanced TVD at intermediate B in the early stages of droplet collision. Furthermore, the enhanced droplet oscillation owing to the unbalanced capillary pressure distributions results in the further increase of TVD at intermediate B in the late stages of droplet collision.

Although the above interpretation provides us a sound description of the observed nonmonotonic viscous dissipation, we found that it is quite phenomenological and has not adequately unveiled the fluid-dynamical physics underlying the problem. Specifically, the TVD is the integration of VDR, $\phi(\boldsymbol{x}, t)$, over the entire droplet volume, V_l, and the entire time duration of droplet bouncing, T, and given by

$$\text{TVD}(\text{T}) = \int_0^{\text{T}} \int_{V_l} \phi(\boldsymbol{x}, t) \, dV \, dt. \tag{1}$$

$\phi(\boldsymbol{x}, t)$ in turn is a complicated nonlinear function of components of strain rate tensor as

$$\phi(\boldsymbol{x}, t) = 2\mu \left[\left(\frac{\partial u}{\partial x} \right)^2 + \left(\frac{\partial v}{\partial y} \right)^2 + \left(\frac{\partial w}{\partial z} \right)^2 \right]$$
$$+ \mu \left[\left(\frac{\partial u}{\partial y} + \frac{\partial v}{\partial x} \right)^2 + \left(\frac{\partial v}{\partial z} + \frac{\partial w}{\partial y} \right)^2 + \left(\frac{\partial w}{\partial x} + \frac{\partial u}{\partial z} \right)^2 \right], \tag{2}$$

where $\boldsymbol{x} = (x, y, z)$ is the coordinate vector and $\boldsymbol{u} = (u, v, w)$ is the velocity vector. It is not physically clear that how the nonmonotonicity is correlated with the unsteady velocity field of droplet internal motion. Apparently, owing to the three-dimensional nature of off-center collision, it is practically clumsy to track the nine velocity gradients in Eq. (2). Applying the principle of Helmholtz decomposition to the droplet internal flow, which is incompressible and, therefore, has a divergence-free velocity field, we can simplify the problem by tracking the vorticity vector. Consequently, we were motivated to further analyze the problem by exploring the vortex-dynamical implications of the nonmonotonic viscous dissipation of off-center droplet bouncing.

First, droplet bouncing was investigated by a few recent studies. Al-Dirawi and Bayly[11] experimentally studied the binary collision between two identical droplets with different viscosities and

proposed an improved model for the prediction of bouncing regimes in the We and B space. Farokhirad et al.[28] and Attarzadeh and Dolatabadi[29] numerically studied the phenomenon of coalescence-induced binary droplets jumping on homogeneous and heterogeneous superhydrophobic surfaces. The dynamics of the interfacial gas layer[30] and viscous effects[31] on the bouncing-to-merging transition in droplets impacting on the liquid film were studied; the droplet impacting on the liquid film can be considered as a limiting case of binary droplet collision with infinite size ratio. Blanchette[32] proposed a model to describe droplet bouncing on an oscillated reservoir with various bouncing modes.

Second, vortex dynamics perspective was adopted by many previous studies[23,33–38] to understand the droplet collision. Behera et al.[33] experimentally studied the effects of drop impingement height and drop shape on the vortex ring formation and explained why a prolate shaped droplet would induce a most penetrating vortex ring. A mechanism based on the generation of vorticity by accelerated flows at curved liquid-free surfaces was proposed to explain the formation of the vortex ring[34,35] upon the droplet merged into a liquid pool.[36] Tsai et al.[38] reported that the traveling of a single large droplet or two-coupled droplets on the oscillatory liquid bath with an inclined bottom was associated with the induced asymmetric vortex flow underneath the liquid surface. Xia et al.[23] interpreted the internal jet formation upon the coalescence of two initially stationary droplets of unequal sizes in terms of main vortex-ring growth and detachment and proposed a vortex-ring-criterion for the appearance of the "mushroom-like" jet. Sun et al.[37] also numerically observed the vortex generation and vortex detachment mechanism to form the internal jet-like mixing between merging droplets, although the intensity of the jet induced by collision at large We is significantly weaker than that induced by surface tension force at small We.

In this paper, we shall present a computational and theoretical study on off-center droplet bouncing with particular interest on analyzing the velocity and vorticity vector fields and their correlations, on unveiling the vortex-dynamical implications of the nonmonotonic TVD with varying impact parameters, and on exploring general characteristics of enstrophy and viscous dissipation for 3D unsteady free-surface flows. To be distinct from the authors' recent study,[27] the significances of the present work are highlighted as follows: (1) correlations between the velocity and vorticity vector fields, such as the helicity (whose integrand is the dot product of velocity and vorticity vectors) and enstrophy (whose integrand is the dot product of vorticity vectors) analysis, were found to be useful measures for 3D droplet internal flow; (2) a general relation between the total enstrophy and the total viscous dissipation rate for an unsteady free-surface flow was theoretically derived and numerically verified; (3) both the total enstrophy and a defined "half-domain" helicity show the nonmonotonic variation with the impact parameter, implying their interrelation with the nonmonotonic viscous dissipation. The numerical methodology and specifications are briefly introduced in Sec. II. The correlation between velocity and vorticity vectors and helicity analysis are given in Sec. III, followed by the enstrophy analysis and its correlation with viscous dissipation in Sec. IV.

II. NUMERICAL METHODOLOGY AND SPECIFICATIONS

A. Numerical method

The continuity and incompressible Navier–Stokes equations,

$$\nabla \cdot \boldsymbol{u} = 0, \qquad (3)$$

$$\rho(\partial \boldsymbol{u}/\partial t + \boldsymbol{u} \cdot \nabla \boldsymbol{u}) = -\nabla p + \nabla \cdot (2\mu \boldsymbol{D}) + \sigma \kappa \boldsymbol{n} \delta_s, \qquad (4)$$

are solved by using the classic fractional-step projection method, where $\boldsymbol{u}$ is the velocity vector, ρ is the density, p is the pressure, μ is the dynamic viscosity, and $\boldsymbol{D}$ is the deformation tensor defined as $D_{ij} = (\partial_j u_i + \partial_i u_j)/2$. In the surface tension term $\sigma \kappa \boldsymbol{n} \delta_s$, δ_s is a Dirac delta function, σ is the surface tension coefficient, κ is the local curvature, and the unit vector $\boldsymbol{n}$ is normal to the local interface.

The present simulation adopts the Volume-of-Fluid (VOF) method. The conventional VOF approach is strongly influenced by the mesh resolution near the interface, and the successful simulation of droplet bouncing requires an extremely fined mesh and thereby a substantial computational cost. Consequently, we adopted the approach of two VOF functions,[39–41] namely, c_1 and c_2, to separately track the interface of each liquid droplet, which can avoid interface coalescence on a coarse mesh. The method with two VOF functions would always enforce droplet bouncing and, thus, is applied in this study to those droplet bouncing cases that have been verified by experiment. It can produce nearly the same droplet deformation and minimum interface distance on relatively coarse mesh as does the conventional VOF approach on a substantially refined mesh. Furthermore, the droplet interfaces can be advected in the two immediately neighboring interface cells, making the minimum interface distance smaller than the minimum mesh size. More details about the VOF methods and their comparison have been sufficiently discussed in our previous paper.[27]

To solve both the gas and liquid phases, the density and viscosity are constructed by the volume fraction as $\rho = (c_1 + c_2)\rho_l + (1 - c_1 - c_2)\rho_g$ and $\mu = (c_1 + c_2)\mu_l + (1 - c_1 - c_2)\mu_g$, in which the subscripts l and g denote the liquid- and gas-phases, respectively. The volume fraction $c_i (i = 1, 2)$ satisfies the advection equation

$$\partial c_i/\partial t + \nabla \cdot (c_i \boldsymbol{u}) = 0, \qquad (5)$$

with $c_i = 1$ for the liquid phase, $c_i = 0$ for the gas phase, and $0 < c_i < 1$ for the gas–liquid interface. The present VOF method had been implemented in the open source code, Gerris,[42,43] featuring the 3D octree adaptive mesh refinement, the geometrical VOF interface reconstruction, and the continuum surface force (CSF) model with height function curvature estimation. Gerris has been demonstrated to be competent for solving a wide range of multiphase flow problems.[19,20,22,23,27,40,44]

B. Numerical specifications and validations

Following the dimensional analysis,[27] the present problem for the off-center bouncing of two droplets of equal size is controlled by three varying parameters, We, Oh, and B, with fixed gas–liquid density and viscosity ratios and a fixed gas pressure. The 3D computational domain is illustrated in Fig. 1. The domain is $6D$ in length and $4D$ in both width and height, and all boundaries are specified
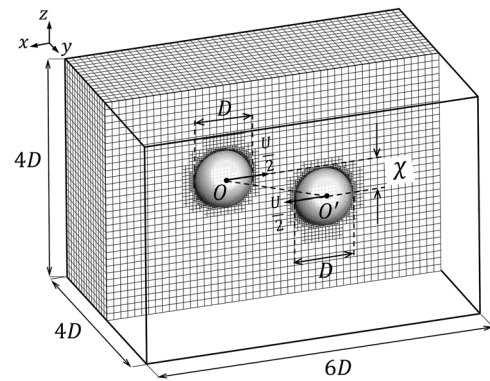

FIG. 1. Computational domain and setup for 3D simulation of off-center droplet collision.

with the free outflow boundary conditions. Two droplets of diameter D are specified to collide along the x-direction with a relative velocity, U, and with zero velocities along the y- and z-directions. The x-velocity component for each droplet has the same magnitude of $U/2$ but opposite sign so that the linear momentum of the entire system remains zero. The x-z plane is established by the x-axis and the connection line denoted as OO', in which O and O' are the mass centers of the colliding droplets. The midpoint of OO' is located at the origin of the Cartesian coordinate system. It is noted that the x-z plane is always a plane of symmetry for the colliding droplets. The deviation of the off-center collision from the head-on collision is qualified by χ, which is defined as the projection of OO' in the z-direction. The non-dimensional time is defined as $T = t/t_{osc}$, where t is the physical time and $t_{osc} = \sqrt{\rho_l D^3/\sigma}$ is proportional to the natural oscillation time of the droplet.

In this study, we used $6 \times 4 \times 4 = 96$ boxes with length L to constitute the entire computational domain, with 6 boxes in the x-direction and 4 boxes in the y- and z-directions, respectively. The droplet diameter is initialized as $D = L$. Given the relative error of integration[45,46] for each dimension $S \approx (\Delta L/L)^{k+1} = 2.2 \times 10^{-9}$, in which $\Delta L = 1/2^7$ is the cell size of the interface zone, $L = 6$ is the domain size, and $k = 2$ is the order of accuracy of the numerical scheme (second-order convergence in space and time of the code, Gerris[42]), the total error is $S_{err} \approx 3S = 6.6 \times 10^{-9}$ for the present three-dimensional problem. The accumulation of errors[45,46] is generally satisfied with $S_{err} \cdot \sqrt{n} \leq S^{max}$, where n is the number of computational time steps and S^{max} is the maximum allowable error that presumed to be between 1% and 5%. Then, the maximum allowable number of computational time steps for solving the present problem can be determined as $n_{max} = (S^{max}/S_{err})^2 = 1.1 \times 10^{13}$. Considering that the total number of time steps is about $n \approx 10\,000$ with the time step about $\Delta t = 2.75 \times 10^{-4}$, the ratio n_{max}/n is thereby sufficiently large to ensure a lower accumulated error and reliable results.

To validate the present numerical setup, the head-on droplet bouncing at two critical transitions We, corresponding to the so-called "soft" and "hard" collisions, and an off-center droplet bouncing have been simulated and compared with the experimental results of Pan et al.[7] and Qian and Law,[5] respectively. To improve

computational efficiency, the computational domain is divided into three physical zones, namely, the gas, the droplet, and the interface, and each zone has its own mesh refinement level denoted by N, which corresponds to a minimum mesh size of $O(2^{-N})$. Accordingly, (N_g, N_d, N_i) is used to describe the refinement level in the three zones. A typical simulation run with the mesh refinement level (3, 5, 7) results in 514 204 grid points in the entire domain, which is equivalent to about 2.0×10^8 grid points if applying a uniform mesh with a size of $O(2^{-7})$. It takes about 100 h of real time to run the simulation up to T = 2.0 on an Intel Xeon(R) E5-2630 processor with 16 cores. As a balance between computational cost and accuracy, the intermediate mesh refinement level of (3, 5, 7) has been used for all simulations. More details about the mesh, experimental validations, and grid independence analysis can be found in our previous paper.[27]

III. DROPLET INTERNAL FLOW, VORTEX LINES, AND HELICITY

A. Velocity and vorticity fields

A representative case of off-center bouncing at $B = 0.3$, $We = 9.3$, and $Oh = 2.8 \times 10^{-2}$ is shown in Fig. 2. To analyze the velocity and vorticity field, the velocity (streamline) and the vorticity magnitude ($|\boldsymbol{\omega}|$) on the symmetry (x-z) plane and on the YOO' plane, where the y-axis and the line OO' lie, are shown in the second and third rows of each time instant. The vorticity vector $\boldsymbol{\omega}$ is given by

$$\boldsymbol{\omega} = \nabla \times \boldsymbol{u} = \left(\frac{\partial w}{\partial y} - \frac{\partial v}{\partial z}, \frac{\partial u}{\partial z} - \frac{\partial w}{\partial x}, \frac{\partial v}{\partial x} - \frac{\partial u}{\partial y} \right). \tag{6}$$

It is seen that the entire collision process can be divided into three stages, namely, the impacting stage (about T = 0.00–0.32) as reaching the maximum droplet deformation driven by the inertia force, the bouncing stage (about T = 0.32–1.00) as recovering to the initial spherical shape driven by the surface tension force, and the oscillating stage (beyond T = 1.00, not included in Fig. 2 for clarity). The large vorticity is normally accompanied by the intensive interface deformation with a large curvature gradient change in the interface. There are two apparent parts of vorticity observed in the vicinity of the droplet interaction region accompanied with the vortical flow, owing to the stretching deformation (as shown by the streamline only for off-center collisions[27]), and in the droplet interior being away from the interaction region close to the interface, respectively. This is qualitatively
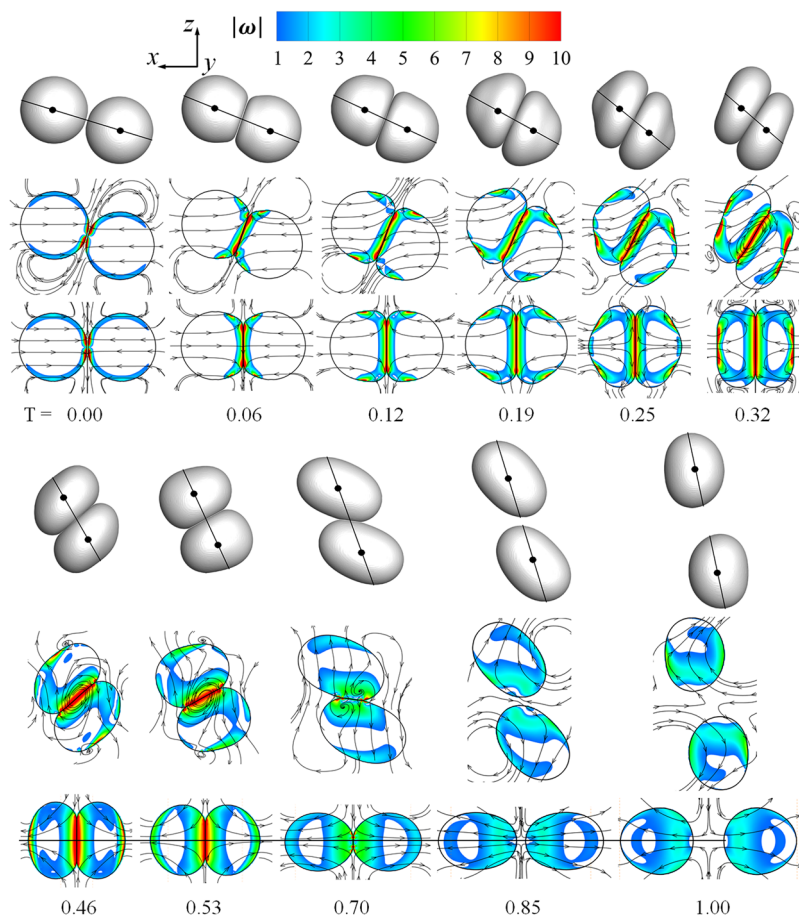

FIG. 2. Droplet deformation, velocity (streamline), and vorticity magnitude ($|\boldsymbol{\omega}|$) field (on the symmetry x-z plane at first two rows and on the plane YOO' consisting of the y-axis and mass center connection line OO' at the last row) for the representative off-center droplet bouncing at $B = 0.3$, $We = 9.3$, and $Oh = 2.8 \times 10^{-2}$. The contours of vorticity have been blanked with a low threshold value of 1.0 for clear comparison.

consistent with the observations of the VDR distribution[27] and implies their possible correlations by the interaction between velocity and vorticity fields.

B. Three-dimensional vortex lines

To better visualize the 3D vorticity field, Fig. 3 shows vortex lines for four cases at $We = 9.3$ and $Oh = 2.8 \times 10^{-2}$ but with different impact parameters. It is seen that the vortex lines for the head-on collision are always a series of concentric circles, which are centered along the line connecting the mass centers of the droplets. This is because the flow is axisymmetric and the vortices are in ring shape. These "ring-shaped" vortices should be attributed to the shear flow formed by the "squeezing" deformation in the axial direction and the "stretching" deformation in the radial direction. For the off-center collision, the "ring-shaped" vortex lines can still be observed in the droplet interior being away from the interaction region between two droplets, although their coaxiality is broken because of the asymmetric shear flow in the radial direction, as shown in the contour at T = 0.12 in Fig. 3.

An interesting finding is the "line-shaped" vortex lines in the vicinity of the droplet interaction region, shown in Fig. 4, which corresponds to a narrow viscous shear layer generated by the stretching deformation of the two droplets. These vortex lines imply that the direction of the shear layer is parallel to both the x-z plane and the droplet interacting surface. We can further observe that both ends of a "line-shaped" vortex line stem from the droplet surface. This can be explained by that, in a finite vorticity field, a vortex filament must either form a closed vortex ring or terminate on the fluid boundaries where the flux of vorticity is not zero.[47]
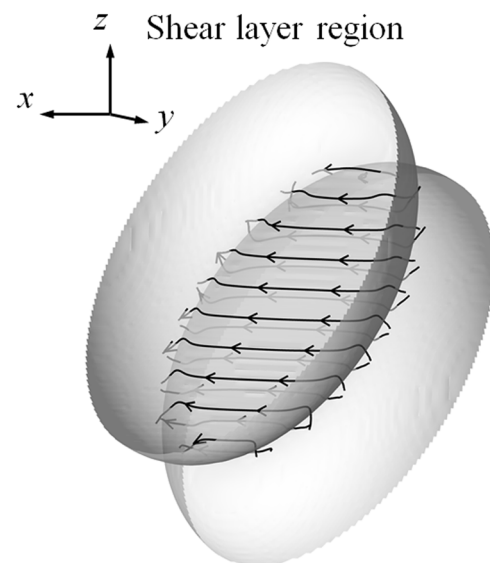

FIG. 4. Close-up of the "line-shaped" shear layers for off-center droplet bouncing.

C. Helicity analysis

The correlation between the vortical structures and the flow field for off-center droplet bouncing can be further understood by considering the "non-orthogonality" of the velocity and vorticity vectors, which is conventionally measured by helicity defined by

$$H = \int \boldsymbol{u} \cdot \boldsymbol{\omega} \, dV, \tag{7}$$
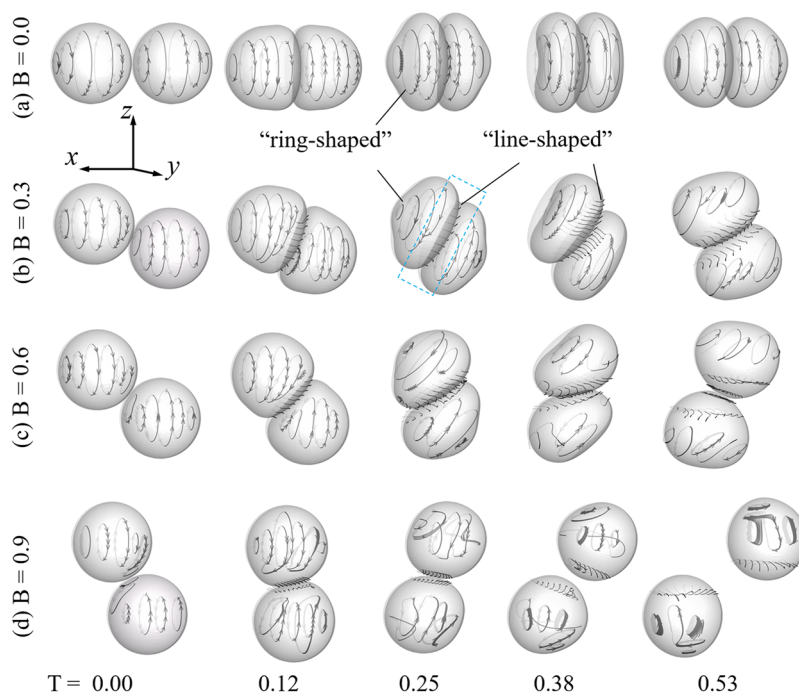

FIG. 3. Evolution of vortex lines between (a) head-on and [(b)–(d)] off-center droplet bouncing for the cases at $We = 9.3$ and $Oh = 2.8 \times 10^{-2}$.
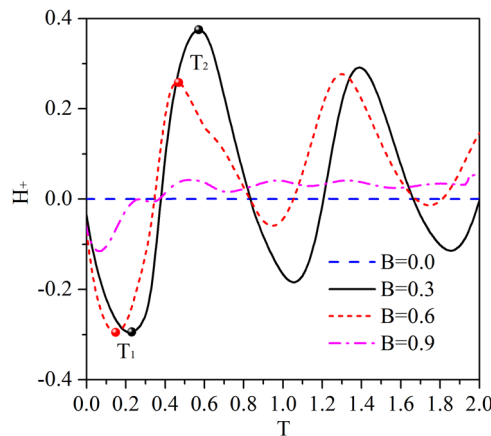
where $\boldsymbol{u} = (u, v, w)$ is the velocity vector and $\boldsymbol{\omega}$ is the vorticity vector given by Eq. (6).

Evidently, the helicity density, $\boldsymbol{u} \cdot \boldsymbol{\omega}$, remains zero everywhere for the head-on collision because the axisymmetric flow has only one vorticity component normal to the velocity plane. The local helicity density is nonzero in general for the off-center collision. However, its integration over the entire droplets [namely, applying Eq. (7) to the droplets] is zero because the x-z plane is always a symmetry plane. The velocity components and the velocity derivatives are reversed on both sides of the x-z plane, expressed as $v_+ = -(v_-)$ and $(\partial/\partial y)_+ = -(\partial/\partial y)_-$, where the positive and negative symbols denote two sides of the x-z plane, respectively. Thus, we have

$$(\boldsymbol{u}_- \cdot \boldsymbol{\omega}_-) = (u, -v, w) \cdot \left(-\frac{\partial w}{\partial y} + \frac{\partial v}{\partial z}, \frac{\partial u}{\partial z} - \frac{\partial w}{\partial x}, -\frac{\partial v}{\partial x} + \frac{\partial u}{\partial y} \right)$$
$$= -(\boldsymbol{u}_+ \cdot \boldsymbol{\omega}_+). \tag{8}$$

Consequently, if we define the "helicity" of liquid droplets in a half space as

$$H_+ = \int_{V_{l_+}} (\boldsymbol{u}_+ \cdot \boldsymbol{\omega}_+) dV, \tag{9a}$$

$$H_- = \int_{V_{l_-}} (\boldsymbol{u}_- \cdot \boldsymbol{\omega}_-) dV, \tag{9b}$$

in which V_{l_+} and V_{l_-} denote the droplet mass on each side of the x-z plane toward positive and negative directions of the y-axis, respectively, we have $H = H_+ + H_- = 0$. The zero integral helicity also indicates that the rotational motion of the entire droplet after off-center collisions that was observed in previous experiments[1-3] and numerical simulations[48] is always perpendicular to the plane that the droplet's mass center trajectory lies, in which the plane must be the symmetry (x-z) plane.[27]

Regardless of the zero helicity, useful information can be obtained by examining either H_+ or H_-. Figure 5 shows the evolution of H_+ with time for different impact parameters. It is seen that H_+ is significantly larger at intermediate B values of 0.3 and 0.6 than at both smaller and larger B, clearly indicating a nonmonotonic
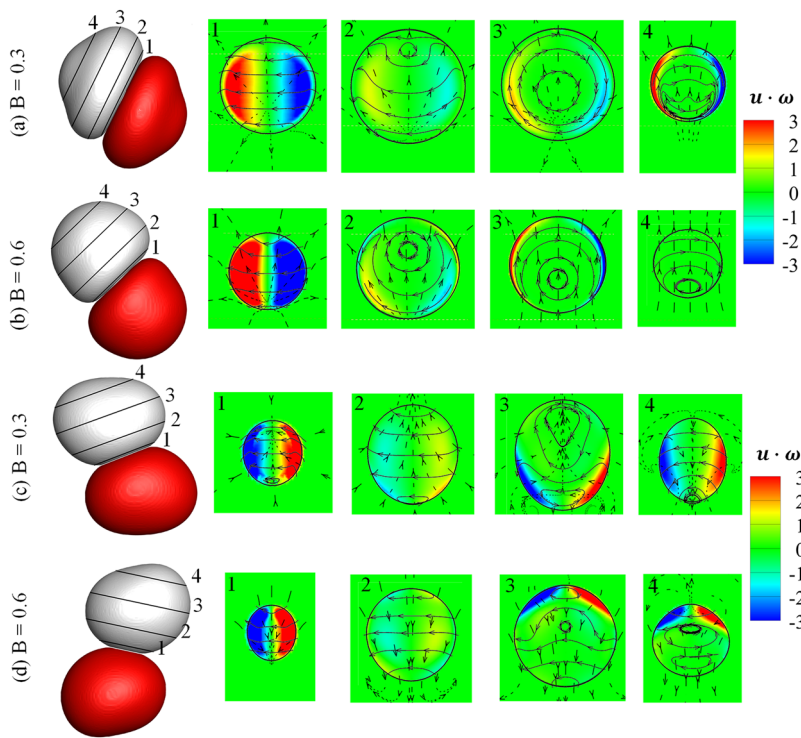

FIG. 6. Contour of helicity density ($\boldsymbol{u} \cdot \boldsymbol{\omega}$), vortex line (solid arrows), and streamline (dashed arrows) on different parallel planes (1–4) for $B = 0.3$ and $B = 0.6$ at two time instants of [(a) and (b)] T_1 and [(c) and (d)] T_2, already indicated in Fig. 5, respectively.

variation of H_+ with an increase in B. This may be understood as that, at intermediate B, both the "ring-shaped" vortices and the "line-shaped" shear layers present a strong influence on their surrounding flows, which translates into strong helicity in the current context. For the cases of small or large B, either "ring-shaped" vortices or the "line-shaped" shear layers are weakened; thus, the entanglement between different types of vortices is suppressed, resulting in the reduced helicity. Furthermore, we note that H_+ can be either positive or negative with several local extrema, owing to the interaction between velocity and vorticity fields, as shown in Fig. 5, in which the values of H_+ at two representative time instants, T_1 and T_2, are the minimum and maximum, respectively.

To further trace the source of helicity, the contours of the helicity density, $\boldsymbol{u} \cdot \boldsymbol{\omega}$, vortex lines, and streamlines on several cross sections parallel to the droplet interacting surface are plotted in Fig. 6 at two time instants, T_1 and T_2, already indicated in Fig. 5, respectively, to show the transition of vortex lines from "line-shaped" to "ring-shaped." We can see that the nonzero $\boldsymbol{u} \cdot \boldsymbol{\omega}$ is mainly distributed in the vicinity of the droplet interaction region or near the interfacial region where the shear layer structure (characterized by the "line-shaped" vortex lines) encounters radial flow induced by the "ring-shaped" vortices. It serves as an indicator of the strong correlation between the velocity field and the vorticity field. For both off-center collisions at $B = 0.3$ and $B = 0.6$, the helicity density on the right-hand part of each slice changes from negative at T_1 to positive at T_2, which is attributed to the change in velocity vectors from droplet impacting to droplet bouncing, but the vorticity vector inside the droplet remains nearly unchanged.

IV. VORTICAL IMPLICATIONS OF VISCOUS DISSIPATION

A. Evolution of Φ and Ψ

As this study was motivated by looking for a possible relation between the non-monotonic viscous dissipation and the vortical flow structure, it is a natural question to ask how to form a scalar quantity based on the velocity and vorticity vectors. In Sec. III, we have shown that the dot product of the velocity and vorticity vectors produces the helicity scalar, which nonmonotonically varies with the impact parameter and, therefore, implies the possible correlation with the viscous dissipation scalar quantity. We recognized that another scalar quantity based on the vorticity vector can be formed by its own dot product, resulting in the well-known enstrophy,[49] defined by

$$\Psi = \int \mu \boldsymbol{\omega} \cdot \boldsymbol{\omega} dV, \qquad (10)$$

where $\boldsymbol{\omega}$ is the vorticity vector given by Eq. (6) and the viscosity coefficient μ is omitted in some definitions.[50]

It is noted that ϕ and ψ have the same dimension, where ϕ is the viscous dissipation rate given by Eq. (2) and $\psi = \mu \omega^2$ is the enstrophy density. Considering an arbitrary closed domain V' confined by stationary boundaries,[49] the total viscous dissipation rate and total enstrophy are the volume integrals of $\Phi = \int_{V'} \phi dV$ and $\Psi = \int_{V'} \psi dV$, respectively. It is well known that $\Phi = \Psi$ holds for a single-phase flow, but it does not guarantee the equality between ϕ and ψ everywhere inside V'.

The evolution of Φ and Ψ for droplet collision is shown in Figs. 7(a) and 7(b), respectively. It is clearly seen that the equality
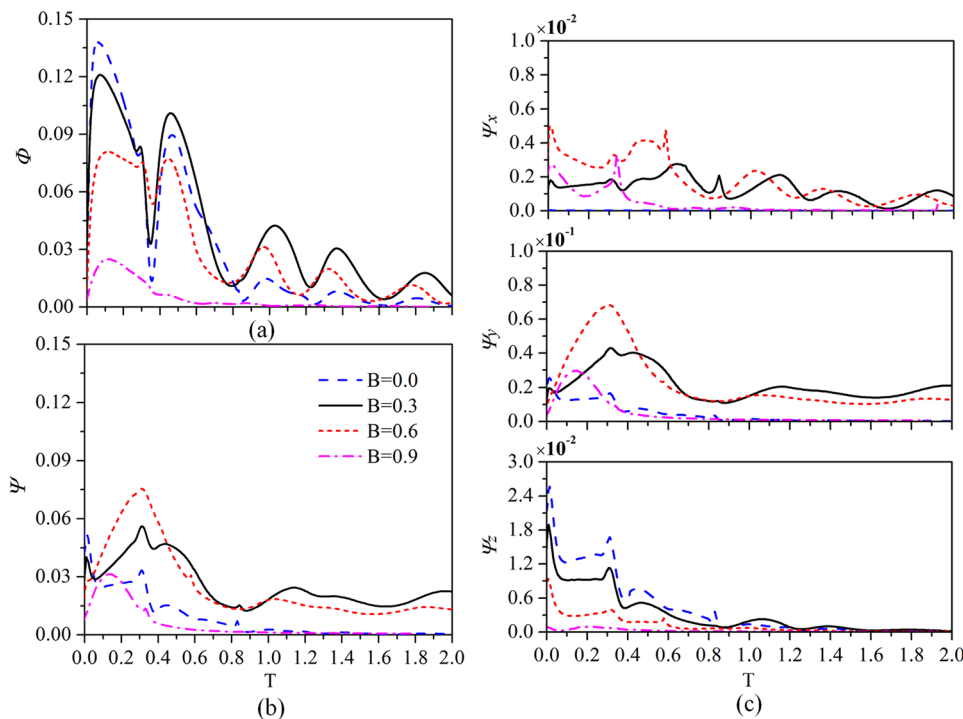

FIG. 7. Evolution of (a) total viscous dissipation rate (Φ), (b) total enstrophy (Ψ), and (c) three scalar parts, Ψ_x, Ψ_y, and Ψ_z, of total Ψ for the cases at $We = 9.3$ and $Oh = 2.8 \times 10^{-2}$.

between Φ and Ψ does not hold because of the presence of the gas–liquid free interface. Φ has one peak value during the impacting stage, one peak value during the bouncing stage, and several peak values during the oscillating stage. However, Ψ shows only one significant peak at the late impacting stage. It is interesting to see that Ψ is enhanced for intermediate B values of 0.3 and 0.6, also showing a nonmonotonic variation with an increase in B. Specifically, Ψ for $B = 0.6$ is larger than other three Bs at early stage, but Ψ for $B = 0.3$ is the largest among all four Bs during the oscillating stage, which is consistent with the previous observation of largest Φ of $B = 0.3$.

It is further noted that the volume integral Ψ can be decomposed into three scalar parts, Ψ_x, Ψ_y, and Ψ_z, which are given by

$$\Psi_x = \int \mu\omega_x^2 dV, \quad \Psi_y = \int \mu\omega_y^2 dV, \quad \Psi_z = \int \mu\omega_z^2 dV. \quad (11)$$

As shown in Fig. 7(c), Ψ_y is about one order larger than Ψ_x and Ψ_z and has nearly the same trend as the total enstrophy Ψ. This indicates that the droplet internal flow responsible for the vorticity vector field is mainly located on these planes that are parallel to the symmetry x-z plane, owing to the stretching deformation in the z-direction by off-center collisions.

B. A general relation between Φ and Ψ

To further understand the difference and similarity between Φ and Ψ, we shall attempt to explore their relation in a general 3D two-phase flow. Following the derivation of Davidson,[49] we found that for the present problem involving gas–liquid interfaces, the relationship between ϕ and ψ could be expressed as

$$\phi - \psi = \nabla \cdot (\mathbf{u} \cdot \boldsymbol{\tau}) - 2\mathbf{u} \cdot \mathbf{D} \cdot \nabla\mu - (\mathbf{u} \times \nabla\mu) \cdot \boldsymbol{\omega} - \nabla \cdot (\mu\mathbf{u} \times \boldsymbol{\omega}), \quad (12)$$

where the viscous stress tensor $\boldsymbol{\tau}$ is related to the strain rate tensor $\mathbf{D}$ as $\boldsymbol{\tau} = 2\mu\mathbf{D}$. Then, we calculated the volume integral of Eq. (12) for the present two-phase flow system shown in Fig. 8, where V' is the
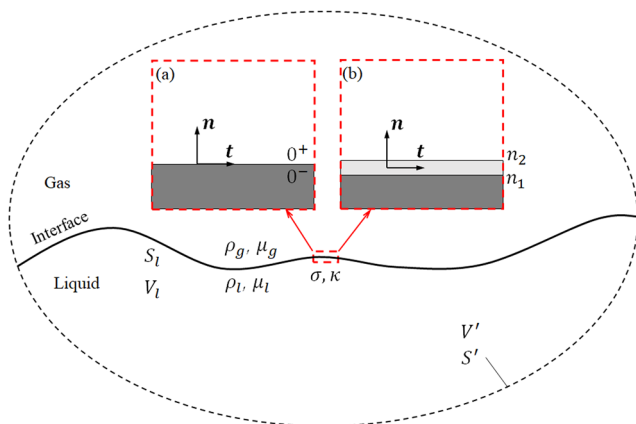

FIG. 8. The schematic of a general two-phase flow system with different models of the (a) ideal interface and (b) numerical interface.

volume of the entire domain including both gas and liquid phases and V_l denotes the volume occupied by the liquid phase enclosed by the surface S_l. V' is assumed to be large enough such that the flow becomes stagnant at the domain boundary S'.

First, we considered the gas–liquid interface S_l as an ideal mathematical interface with discontinuous properties across it, as illustrated in Fig. 8(a). Then, the integrals associated with $2\mathbf{u} \cdot \mathbf{D} \cdot \nabla\mu$ and $(\mathbf{u} \times \nabla\mu) \cdot \boldsymbol{\omega}$ vanish because $\nabla\mu = 0$ is satisfied in both liquid- and gas-phases constituting the entire integral domain V'. To obtain the volume integrals of $\nabla \cdot (\mathbf{u} \cdot \boldsymbol{\tau})$ and $\nabla \cdot (\mu\mathbf{u} \times \boldsymbol{\omega})$, we noted that the Gauss theorem in the present case takes the form of

$$\int_{V'} \nabla \cdot \mathbf{F} dV = \oint_{S'} \mathbf{F} \cdot \mathbf{n} dA - \oint_{S_l} [\![\mathbf{F} \cdot \mathbf{n}]\!]_s dA, \quad (13)$$

where the jump of a function g is defined as $[\![g]\!]_s = g(n = 0^+) - g(n = 0^-)$, with $n = 0$ denoting the location of the free interface S_l, as shown in Fig. 8(a).

Applying Eq. (13), the volume integral of $\nabla \cdot (\mathbf{u} \cdot \vec{\vec{\tau}})$ can be derived as

$$\int_{V'} \nabla \cdot (\mathbf{u} \cdot \boldsymbol{\tau}) dV = -\oint_{S_l} [\![\mathbf{u} \cdot \boldsymbol{\tau} \cdot \mathbf{n}]\!]_S dA = \oint_{S_l} ([\![p]\!]_S - \sigma\kappa) u_n dA, \quad (14)$$

where the surface integral on S' is eliminated because of the stagnation boundary condition. The second equation of Eq. (14) is derived by taking advantage of the stress boundary conditions across the free interface[51] S_l that $[\![\mathbf{t} \cdot \boldsymbol{\tau} \cdot \mathbf{n}]\!]_S = 0$ and $[\![\mathbf{n} \cdot \boldsymbol{\tau} \cdot \mathbf{n}]\!]_S = -[\![p]\!]_S + \sigma\kappa$, where $\mathbf{n}$ and $\mathbf{t}$, respectively, denote the unit vectors in the normal and tangential directions of S_l. So, $u_n = \mathbf{u} \cdot \mathbf{n}$ is the normal velocity component of S_l.

Similarly, the integral of $\nabla \cdot (\mu\mathbf{u} \times \boldsymbol{\omega})$ can be derived as

$$\int_{V'} \nabla \cdot (\mu\mathbf{u} \times \boldsymbol{\omega}) dV = -\oint_{S_l} [\![\mu(\mathbf{u} \times \boldsymbol{\omega}) \cdot \mathbf{n}]\!]_S dA = \oint_{S_l} [\![\mu\omega]\!]_S u_t dA, \quad (15)$$

where $\boldsymbol{\omega} = \omega(\mathbf{t} \times \mathbf{n})$ and $u_t = \mathbf{u} \cdot \mathbf{t}$ is the velocity component in the tangential direction of the interface S_l. It is noted that the derivation of Eq. (15) requires the no-slip boundary condition at the gas–liquid interface so that u_t is continuous across S_l.

We combined Eqs. (12), (14), and (15) to have

$$\int_{V'} (\phi - \psi) dV = \oint_{S_l} (([\![p]\!]_S - \sigma\kappa) u_n + \mu_l \omega_l u_t) dA, \quad (16)$$

where $[\![p]\!]_S$ denotes the pressure jump across the interface S_l; u_n and u_t are the normal and tangential velocity components, respectively; and ω_l is the vorticity in the liquid phase. The $\mu\omega u_t$ term pertaining to the gas phase is dropped out because of the negligible gas viscosity compared with fluid viscosity.

Furthermore, we noted that the interface between different phases is modeled by a VOF method as a finite-thickness surface with continuously varying properties in the normal direction, as illustrated in Fig. 8(b). Thus, the interface location in the normal direction is extended from $n = 0$ to $[n_1, n_2]$, where $n_1 < 0$ to $n_2 > 0$. In this case, the Gauss theorem has its original form so that the volume integrations of $\nabla \cdot (\mathbf{u} \cdot \boldsymbol{\tau})$ and $\nabla \cdot (\mu\mathbf{u} \times \boldsymbol{\omega})$ vanish again.[49] However, since $\nabla\mu$ now becomes finite throughout the finite-thickness
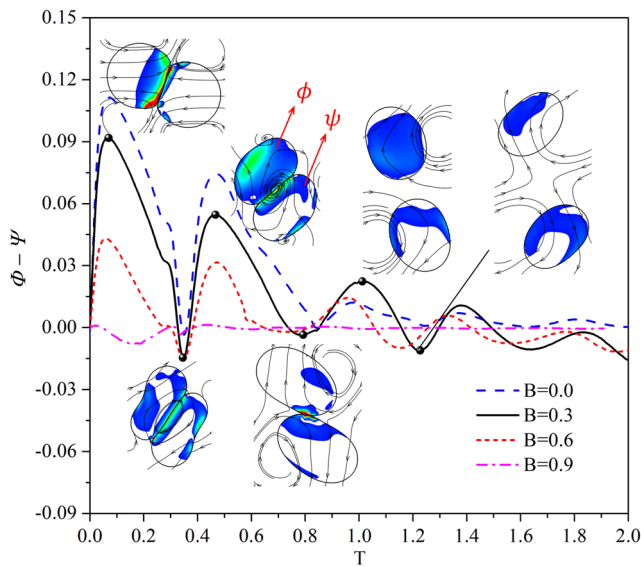
FIG. 9. Comparison of the deviation of $\Phi - \Psi$ for different impact parameters. The imbedded pictures are the local ϕ and ψ for the representative case of $B = 0.3$, $We = 9.3$, and $Oh = 2.8 \times 10^{-2}$ at each local extremum.

interface, the integrations of $2\boldsymbol{u} \cdot \boldsymbol{D} \cdot \nabla\mu$ and $(\boldsymbol{u} \times \nabla\mu) \cdot \boldsymbol{\omega}$ can be, respectively, derived as

$$\int_{V'} 2\boldsymbol{u} \cdot \boldsymbol{D} \cdot \nabla\mu \, \mathrm{d}V = \oint_{S_l} \int_{n_1}^{n_2} 2\boldsymbol{u} \cdot \boldsymbol{D} \cdot \boldsymbol{n} \frac{\partial\mu}{\partial n} \mathrm{d}n \mathrm{d}A = \oint_{S_l} [\![\boldsymbol{u} \cdot \boldsymbol{\tau} \cdot \boldsymbol{n}]\!]_S \mathrm{d}A$$

$$(17)$$

and

$$\int_{V'} (\boldsymbol{u} \times \nabla\mu) \cdot \boldsymbol{\omega} \, \mathrm{d}V = \oint_{S_l} \int_{n_1}^{n_2} (\boldsymbol{u} \times \boldsymbol{n}) \cdot \boldsymbol{\omega} \frac{\partial\mu}{\partial n} \mathrm{d}n \mathrm{d}A$$

$$= -\oint_{S_l} [\![\mu(\boldsymbol{u} \times \boldsymbol{\omega}) \cdot \boldsymbol{n}]\!]_S \mathrm{d}A, \quad (18)$$

where the jump of g here is defined as $[\![g]\!]_S = g(n = n_2) - g(n = n_1)$. Combining Eqs. (12), (17), and (18), we again attained Eq. (16).

The physical meaning of Eq. (16) describes that the deviation between Φ and Ψ for two-phase flow is attributed to two sources at the gas–liquid interface: the first is related to the work done by the normal component of the viscous stress, which equals $[\![p]\!]_S - \sigma\kappa$, and the second is related to the work done by a virtual shear stress, $\mu_l\omega_l$. It should be noted that, in this study, the outer air phase is insignificant and has a negligible effect on momentum or energy
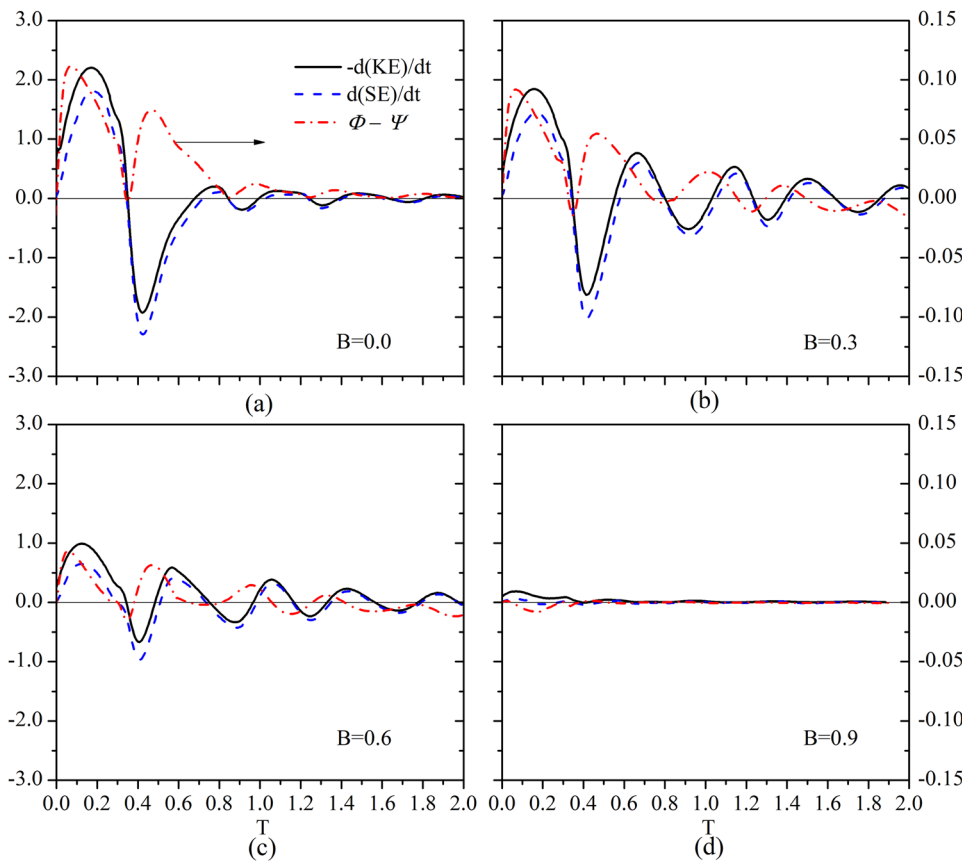

FIG. 10. Relations between $\Phi - \Psi$, change rates of kinetic energy, $-\mathrm{d}(KE)/\mathrm{d}t$, and surface energy, $\mathrm{d}(SE)/\mathrm{d}t$, at $We = 9.3$ and $Oh = 2.8 \times 10^{-2}$ for (a) $B = 0.0$, (b) $B = 0.3$, (c) $B = 0.6$, and (d) $B = 0.9$, respectively.

transfer, owing to the large liquid-to-gas ratios of density and viscosity. Thus, the free outflow boundaries in simulations may be considered as approximately stationary boundaries without losing much accuracy in the liquid phase.

C. Evolution of $\Phi - \Psi$ for droplet bouncing

Figure 9 shows the evolution of $\Phi - \Psi$ for different impact parameters. Snapshots of contours of local ϕ and ψ at the x-z plane are plotted at the instants corresponding to local maxima and minima of the main curve for the representative case of $B = 0.3$. Figure 9 verifies that $\Phi - \Psi$ is indeed non-zero for the present two-phase flow problem as predicted by Eq. (16). It can be further observed that $\Phi - \Psi$ oscillates and the amplitude decreases gradually after several periods of droplet oscillation, in a manner similar to the evolution of Φ shown in Fig. 7, and with the same time instants for each local extremum. It is, therefore, consistent with the interpretation from Eq. (16) that $\Phi - \Psi$ is closely related to the interfacial movement, which is synchronized with the oscillation of the entire droplet.

To further verify the correlation between $\Phi - \Psi$ and droplet interfacial movement, we plotted $\Phi - \Psi$, the change rates of the normalized kinetic energy (KE) and surface energy (SE) for different impact parameters in Fig. 10. It shows that the KE and the SE always change synchronously during the droplet collision process, and their difference is the total viscous dissipation rate. For the head-on collision, as shown in Fig. 10(a), the time instants with $\Phi - \Psi = 0$ and those with $d(\text{SE})/dt = -d(\text{KE})/dt = 0$ corresponding to the maximum droplet deformation are approximately matched, indicating that $\Phi - \Psi = 0$ occurs at maximum droplet deformation and thereby nearly stationary interfacial movement. However, the mismatch between the time instants with $d(\text{SE})/dt = -d(\text{KE})/dt = 0$ and $\Phi - \Psi = 0$ for off-center collisions, as shown in Figs. 10(b)–10(d), is observed and probably attributed to the fact that maximum droplet deformation does not guarantee stationary interfacial movement everywhere for any stretching or oscillating droplets, hence resulting in a hysteresis between the zero points.

V. CONCLUDING REMARKS

To further understand our previous finding of the nonmonotonic viscous dissipation[27] with varying impact parameters for the off-center droplet bouncing, the vortex-dynamical implications of this finding were explored by computationally and theoretically analyzing the velocity and vorticity vector fields and their correlations.

The helicity analysis provides a correlation between velocity and vorticity fields, which shows similar nonmonotonicity of the viscous dissipation. The local helicity density is zero for the head-on collision because of the axisymmetric flow with only "ring-shaped" vortices, but it is nonzero for off-center collisions. Although the integral helicity over the entire droplets is zero due to the presence of the symmetry plane, the nonzero "half-domain" source helicity is mainly distributed in the vicinity of the droplet interaction region or the interfacial region with the strong interaction between the "ring-shaped" vortices and the "line-shaped" shear layers. Such an interaction becomes significant at intermediate impact parameters.

The enstrophy analysis provides another correlation between velocity and vorticity vectors, which again shows a nonmonotonicity trend with an increase in the impact parameter. We derived a general relation between the total enstrophy (Ψ) and the total viscous dissipation rate (Φ) for the unsteady free-surface flow. The important conclusion from the derivation is that Ψ is generally different from Φ in a two-phase flow, whereas there is equality between the two terms for a single-phase flow. This difference is analytically attributed to two terms that originated from the phase interface: the work done by the viscous stress along the normal direction and the work done by the virtual shear stress along the tangential direction. Both terms are caused by the unbalanced flow and vorticity across the interface, and the deviation of $\Phi - \Psi$ is verified to be closely related to the interfacial movement in this study of off-center droplet bouncing.

Although there is no exact one-to-one correspondence of time evolution between the total viscous dissipation rate, the total enstrophy, and the helicity, they all show the same nonmonotonic variation with B, which verifies the hypothesis that motivated this study. Future studies are merited to understand other three-dimensional droplet impact problems from the present vortex-dynamical perspectives.

REFERENCES

[1]P. Brazier-Smith, S. Jennings, and J. Latham, "The interaction of falling water drops: Coalescence," Proc. R. Soc. London, Ser. A **326**, 393 (1972).

[2]S. Bradley and C. Stow, "Collisions between liquid drops," Proc. R. Soc. London, Ser. A **287**, 635 (1978).

[3]N. Ashgriz and J. Poo, "Coalescence and separation in binary collisions of liquid drops," J. Fluid Mech. **221**, 183 (1990).

[4]Y. J. Jiang, A. Umemura, and C. K. Law, "An experimental investigation on the collision behavior of hydrocarbon droplets," J. Fluid Mech. **234**, 171 (1992).

[5]J. Qian and C. K. Law, "Regimes of coalescence and separation in droplet collision," J. Fluid Mech. **331**, 59 (1997).

[6]J.-P. Estrade, H. Carentz, G. Lavergne, and Y. Biscos, "Experimental investigation of dynamic binary collision of ethanol droplets—A model for droplet coalescence and bouncing," Int. J. Heat Fluid Flow **20**, 486 (1999).

[7]K.-L. Pan, C. K. Law, and B. Zhou, "Experimental and mechanistic description of merging and bouncing in head-on binary droplet collision," J. Appl. Phys. **103**, 064901 (2008).

[8]C. Tang, P. Zhang, and C. K. Law, "Bouncing, coalescence, and separation in head-on collision of unequal-size droplets," Phys. Fluids **24**, 022101 (2012).

[9]M. Sommerfeld and M. Kuschel, "Modelling droplet collision outcomes for different substances and viscosities," Exp. Fluids **57**, 187 (2016).

[10]G. Finotello, R. F. Kooiman, J. T. Padding, K. A. Buist, A. Jongsma, F. Innings, and J. Kuipers, "The dynamics of milk droplet–droplet collisions," Exp. Fluids **59**, 17 (2018).

[11]K. H. Al-Dirawi and A. E. Bayly, "A new model for the bouncing regime boundary in binary droplet collisions," Phys. Fluids **31**, 027105 (2019).

[12]M. Orme, "Experiments on droplet collisions, bounce, coalescence and disruption," Prog. Energy Combust. Sci. **23**, 65 (1997).

[13]G. Brenn, "Droplet collision," in *Handbook of Atomization and Sprays* (Springer, Berlin, 2011).

[14]H. P. Kavehpour, "Coalescence of drops," Annu. Rev. Fluid Mech. **47**, 245 (2015).

[15]N. Roth, C. Rabe, B. Weigand, F. Feuillebois, and J. Malet, "Droplet collision outcomes at high Weber number," in *Proceedings of the 21st Conference* (Institute for Liquid Atomization and Spray Systems, 2007).

[16]K.-L. Pan, P.-C. Chou, and Y.-J. Tseng, "Binary droplet collision at high Weber number," Phys. Rev. E **80**, 036301 (2009).

[17]G. Finotello, J. T. Padding, N. G. Deen, A. Jongsma, F. Innings, and J. Kuipers, "Effect of viscosity on droplet-droplet collisional interaction," Phys. Fluids **29**, 067102 (2017).

[18]C. Gotaas, P. Havelka, H. A. Jakobsen, H. F. Svendsen, M. Hase, N. Roth, and B. Weigand, "Effect of viscosity on droplet-droplet collision outcome: Experimental study and numerical comparison," Phys. Fluids **19**, 102106 (2007).

[19]X. Chen, D. Ma, P. Khare, and V. Yang, "Energy and mass transfer during binary droplet collision," in *49th AIAA Aerospace Sciences Meeting* (AIAA, 2011).

[20]X. Chen, D. Ma, and V. Yang, "Collision outcome and mass transfer of unequal-sized droplet collision," in *50th AIAA Aerospace Sciences Meeting* (AIAA, 2012).

[21]H. Deka, G. Biswas, S. Chakraborty, and A. Dalal, "Coalescence dynamics of unequal sized drops," Phys. Fluids **31**, 012105 (2019).

[22]C. Tang, J. Zhao, P. Zhang, C. K. Law, and Z. Huang, "Dynamics of internal jets in the merging of two droplets of unequal sizes," J. Fluid Mech. **795**, 671 (2016).

[23]X. Xia, C. He, D. Yu, J. Zhao, and P. Zhang, "Vortex-ring-induced internal mixing upon the coalescence of initially stationary droplets," Phys. Rev. Fluids **2**, 113607 (2017).

[24]Z. Zhang, Y. Chi, L. Shang, P. Zhang, and Z. Zhao, "On the role of droplet bouncing in modeling impinging sprays under elevated pressures," Int. J. Heat Mass Transfer **102**, 657 (2016).

[25]Z. Zhang and P. Zhang, "Cross-impingement and combustion of sprays in high-pressure chamber and opposed-piston compression ignition engine," Appl. Therm. Eng. **144**, 137 (2018).

[26]Z. Zhang and P. Zhang, "Modeling kinetic energy dissipation of bouncing droplets for Lagrangian simulation of impinging sprays under high ambient pressure," Atomization Sprays **28**, 673 (2018).

[27]C. He, X. Xia, and P. Zhang, "Non-monotonic viscous dissipation of bouncing droplets undergoing off-center collision," Phys. Fluids **31**, 052004 (2019).

[28]S. Farokhirad, J. F. Morris, and T. Lee, "Coalescence-induced jumping of droplet: Inertia and viscosity effects," Phys. Fluids **27**, 102102 (2015).

[29]R. Attarzadeh and A. Dolatabadi, "Coalescence-induced jumping of micro-droplets on heterogeneous superhydrophobic surfaces," Phys. Fluids **29**, 012104 (2017).

[30]X. Tang, A. Saha, C. K. Law, and C. Sun, "Bouncing drop on liquid film: Dynamics of interfacial gas layer," Phys. Fluids **31**, 013304 (2019).

[31]X. Tang, A. Saha, C. K. Law, and C. J. L. Sun, "Bouncing-to-merging transition in drop impact on liquid film: Role of liquid viscosity," Langmuir **34**, 2654 (2018).

[32]F. Blanchette, "Modeling the vertical motion of drops bouncing on a bounded fluid reservoir," Phys. Fluids **28**, 032104 (2016).

[33]M. R. Behera, A. Dasgupta, and S. Chakraborty, "On the generation of vorticity and hydrodynamics of vortex ring during liquid drop impingement," Phys. Fluids **31**, 082108 (2019).

[34]R. Cresswell and B. Morton, "Drop-formed vortex rings—The generation of vorticity," Phys. Fluids **7**, 1363 (1995).

[35]T. Lundgren and P. Koumoutsakos, "On the generation of vorticity at a free surface," J. Fluid Mech. **382**, 351 (1999).

[36]P. Shankar and M. Kumar, "Vortex rings generated by drops just coalescing with a pool," Phys. Fluids **7**, 737 (1995).

[37]K. Sun, P. Zhang, M. Jia, and T. Wang, "Collision-induced jet-like mixing for droplets of unequal-sizes," Int. J. Heat Mass Transfer **120**, 218 (2018).

[38]M.-H. Tsai, K. L. Law, and H.-Y. Chu, "Asymmetric vortexes induced traveling drop on an oscillatory liquid bath," Phys. Fluids **31**, 102102 (2019).

[39]E. Coyajee and B. J. Boersma, "Numerical simulation of drop impact on a liquid–liquid interface with a multiple marker front-capturing method," J. Comput. Phys. **228**, 4444 (2009).

[40]C. Hu, S. Xia, C. Li, and G. Wu, "Three-dimensional numerical investigation and modeling of binary alumina droplet collisions," Int. J. Heat Mass Transfer **113**, 569 (2017).

[41]M. Kwakkel, W.-P. Breugem, and B. J. Boersma, "Extension of a CLSVOF method for droplet-laden flows with a coalescence/breakup model," J. Comput. Phys. **253**, 166 (2013).

[42]S. Popinet, "An accurate adaptive solver for surface-tension-driven interfacial flows," J. Comput. Phys. **228**, 5838 (2009).

[43]S. Popinet, "Numerical models of surface tension," Annu. Rev. Fluid Mech. **50**, 49 (2018).

[44]X. Xia, C. He, and P. Zhang, "Universality in the viscous-to-inertial coalescence of liquid droplets," Proc. Natl. Acad. Sci. U. S. A. **116**, 23467 (2019).

[45]N. Smirnov, V. Betelin, V. Nikitin, L. Stamov, and D. Altoukhov, "Accumulation of errors in numerical simulations of chemically reacting gas dynamics," Acta Astronaut. **117**, 338 (2015).

[46]N. Smirnov, V. Betelin, R. Shagaliev, V. Nikitin, I. Belyakov, Y. N. Deryuguin, S. Aksenov, and D. Korchazhkin, "Hydrogen fuel rocket engines simulation using LOGOS code," Int. J. Hydrogen Energy **39**, 10748 (2014).

[47]P. G. Saffman, *Vortex Dynamics* (Cambridge University Press, 1992).

[48]K.-L. Pan, K.-L. Huang, W.-T. Hsieh, and C.-R. Lu, "Rotational separation after temporary coalescence in binary droplet collisions," Phys. Rev. Fluids **4**, 123602 (2019).

[49]P. A. Davidson, *Turbulence: An Introduction for Scientists and Engineers* (Oxford University Press, 2015).

[50]C. R. Doering, J. D. Gibbon, and J. Gibbon, *Applied Analysis of the Navier-Stokes Equations* (Cambridge University Press, 1995).

[51]G. Tryggvason, "Direct numerical simulations of gas–liquid flows," in *Multiphase Flow Handbook* (CRC Press, Boca Raton, FL, 2016), Chap. 2.2, p. 95.